EVALUATION OF AN UNSTEADY PANEL METHOD FOR THE PREDICTION OF ROTOR-ROTOR AND ROTOR-BODY INTERACTIONS IN PRELIMINARY DESIGN

Philipp Kunze
Deutsches Zentrum für Luft- und Raumfahrt e.V. (DLR)
Institute of Aerodynamics and Flow Technology, Braunschweig, Germany

Abstract

The DLR unsteady panel and free-wake code UPM is evaluated for the prediction of rotor-rotor and rotor-body interactions in preliminary design. Therefore, several well-known test cases are selected and used to compare the numerical results with experimental data. The test cases regard a tandem rotor in hover with varying rotor overlap, the performance of a tandem and a coaxial rotor in level flight and on the rotor-body interference and its effect on the rotor inflow and wake. For the proper simulation of the experiments, routines for trimming of dual rotor configurations and for the estimation of profile power were implemented. In course of the investigations, best practices for the application of UPM for interference calculations in predesign were derived, aimed at ensuring accurate results while minimizing the computational costs. Regarding the selected test cases, most of the simulation results show an excellent agreement with experimental data, both qualitatively and quantitatively. The results encourage the integration of UPM into the DLR predesign framework, enabling a physics-based consideration of many steady and unsteady interference effects in this early design stage. Nevertheless, the computational expense of the free-wake method is considerably higher compared to conventional predesign methods and exceeds a practical level for direct integration into design optimization loops. Thus, alternative approaches for the integration of UPM into the preliminary design toolchain are proposed.

1. NOMENCLATURE

A	rotor disk area
c	rotor blade chord length
c_d	sectional profile drag coefficient
c_l	sectional lift coefficient
$c_{l,\alpha=0}$	sectional lift coefficient at zero angle of attack
C_P	rotor power coefficient
C_Q	rotor torque coefficient
C_T	rotor thrust coefficient
$dc_l/d\alpha$	aifoil lift curve slope
d	horizontal rotor distance
D	rotor diameter
f	equivalent fuselage flat-plate drag area
K_0, K_1	parameters for profile drag approximation
M_{tip}	rotor blade tip Mach number
$M_{x/y/z}$	roll/pitch/yaw moment
N_b	number of blades
r	radial coordinate
R	rotor radius
t/c	relative airfoil thickness
T	rotor thrust
v_{tip}	rotor blade tip speed
v_∞	flight speed / onflow velocity
Δz	vertical rotor separation
α	angle of attack
α_{TPP}	tip path plane tilt angle
α_s	rotor shaft tilt angle
β_0	coning angle
λ	rotor blade taper ratio
λ_i	induced inflow normal to TPP (pos. downwards)
μ	advance ratio
μ_i	induced inflow tangential (streamwise) to TPP
$\theta_{0/1s/1c}$	collective / lateral / longitudinal pitch angle
ψ	azimuth angle
2MRTS	2-Meter Rotor Test System
BVI	Blade Vortex Interaction
CoG	Center of Gravity
HOST	Helicopter Overall Simulation Tool
LV	Laser Velocimetry
rev	revolution
rpm	revolutions per minute
TPP	Tip Path Plane
UPM	Unsteady Panel Method

2. INTRODUCTION

Interference effects can have a great impact on the overall performance and loads of rotorcraft [1]. Therefore they should already be taken into account in the early design stages. This is especially true for configurations, where rotors or propellers operate in the wakes of other components, causing strong mutual interactions, e.g. multi-rotor configurations (coaxial, tandem) and compound helicopters. During preliminary design interference effects are usually estimated using low-order physics-based methods (e.g. momentum theory), experimental results or derived semi-empirical methods. But these methods fail to predict unsteady loads, as formation and development of rotor wakes in time are not considered. Moreover the effect of complex body shapes in the vicinity of rotors on the flow field and its adverse interference are not taken into account. On the other hand, computation times for higher fidelity methods based on potential flow and free-wake models, which are able to accurately predict unsteady loads and wake interaction effects in many cases, are continuously decreasing due to increasing computer performance and advances in parallel computing and algorithms. Thus, the feasibility of the use of such an unsteady panel method for the calculation of interference effects during preliminary design is assessed in this paper. Therefore several rotor-rotor and rotor-body interaction test cases have been selected to evaluate this method in terms of result quality, robustness and computational performance.

3. COMPUTATIONAL METHOD

3.1. Unsteady Panel Method (UPM)

The unsteady three-dimensional panel free wake code UPM [2] [3], developed at the DLR Institute of Aerodynamics and Flow Technology, is used for all numerical simulations presented in this work. UPM implements a velocity-based, indirect potential formulation. Lifting surfaces, i.e. rotor blades and wings, are modelled by a vortex-lattice on the camber surface combined with constant source/sink surface panels in order to account for both lift and thickness effects. From the Kutta panels at the trailing edge of lifting surfaces, a full-span free wake consisting of connected vortex filaments is shed, as shown by the red lines in Figure 2. The wake growth and shape is calculated by explicit time-stepping. Non-lifting bodies are modelled using quadrilateral surface panels (Figure 1) with constant source/sink strength, only taking into account the displacement of the flow caused by these components, while neglecting the generation of lift and drag.

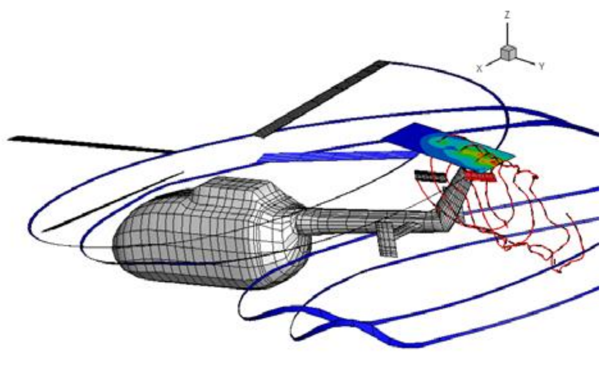

Figure 1: Example of an unsteady UPM simulation of a full configuration, including main rotor, tail rotor and fuselage [3]

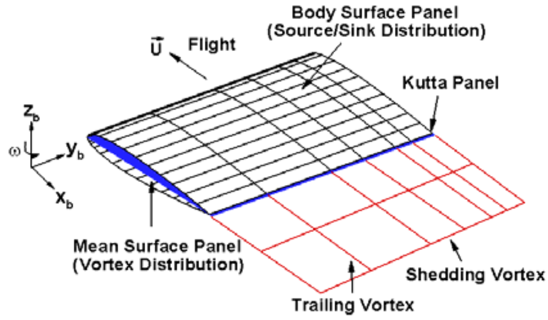

Figure 2: Modeling of lifting surfaces in UPM [3]

Aside from that, a compressibility correction option based on the section-wise application of the Prandtl-Glauert method and a simple internal trim procedure using the Newton-Raphson method are available in UPM. Furthermore, there are routines for coupling UPM with Airbus Helicopters' Helicopter Overall Simulation Tool (HOST), which allow to incorporate flight dynamics, advanced trim laws and elastic blade deformation in the simulations.

All calculations for the work presented in this paper were performed assuming rigid blades. Custom trim procedures for tandem and coaxial rotors were implemented in external Python scripts wrapped around UPM. Additional data extraction and post processing routines were also implemented in Python.

3.2. Viscous profile power estimation

The viscous profile power of rotors is included in the results by incorporating drag coefficient data as a function of local angle of attack, Mach and Reynolds number and taking into account the required power from the resulting local profile drag forces during one rotor revolution. The local angle of attack is estimated from the sectional lift coefficient and two-dimensional airfoil characteristics ($dc_l/d\alpha$, $c_{l,\alpha=0}$) defined in the user input, using the following relation based on the assumption of a linear lift curve:

$$\alpha = \frac{c_l - c_{l_{\alpha=0}}}{dc_l \,/\, d\alpha} \tag{1}$$

The sectional lift coefficient is approximated by the sectional normal coefficient calculated by UPM. Two profile drag models are readily available. Firstly, a very simple model assuming a constant profile drag coefficient, independent from the local sectional onflow conditions:

$$c_d = c_{d0} = const. \tag{2}$$

Secondly, a profile drag model based on the interpolation of drag data from airfoil lookup tables:

$$c_d = f(\alpha, Ma, Re) \tag{3}$$

Other profile drag models can be implemented easily as a custom function of angle of attack, Mach and Reynolds number or a subset of these inputs. For the tandem and coaxial rotor power calculations in this paper, a method similar to [4] was implemented and applied. The sectional profile drag coefficient was modelled as a function of the local angle of attack:

$$c_d = f(\alpha) = \max(K_0, K_1 \cdot (1 - \cos(\alpha + \alpha_0))) \tag{4}$$

The model was calibrated for each rotor by calculating K_0, K_1 and α_0 using nonlinear least squares approximation with available experimental rotor hover static thrust data as reference. The two-dimensional airfoil characteristics ($dc_l/d\alpha = 6.91$, $c_{l,\alpha=0} = 0$) used for the estimation of the local angle of attack were obtained from incompressible and inviscid potential flow simulations of the NACA0012 airfoil using XFOIL [5], since all rotors considered in this work have symmetrical 4-digit NACA airfoil sections.

4. RESULTS

Several well-known dual rotor and rotor-fuselage interaction test cases were selected and used for the evaluation of UPM. The results are presented in the following sections.

4.1. Tandem rotor thrust in hover

The first test case is based on experimental investigations of tandem rotors in hover by Stepniewski, conducted in 1947. The experimental data were published in [6]. Stepniewski's tandem rotor model consisted of two coplanar rotors with three untwisted rectangular blades each. The rotor blades with a radius of 1.23 m and 0.04 m chord length were equipped with symmetrical NACA0012 airfoils. The tandem rotor was tested for various collective pitch angles, blade tip Mach numbers and rotor overlap (defined as $1 - d/D$) values. More detailed geometrical specifications and operating conditions are shown in Figure 3 and Table 1.

Table 1: Tandem rotor parameters

Property	Symbol	Value	Unit
rotor distance	d/D	0.625 ... 1.0365	[-]
vertical separation	$\Delta z/D$	0.0	[%]
number of blades / rotor	N_b	3	[-]
radius	R	1.23	[m]
blade chord length	c	0.04	[m]
taper ratio	λ	1.0	[-]
Twist	$\Delta\theta$	0.0	[°]
tip Mach number	M_{tip}	0.36 ... 0.46	[-]

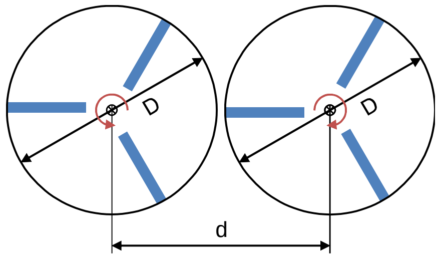

Figure 3: Tandem rotor geometry specifications

Initial studies involving UPM simulations of the isolated front and rear rotors showed that the calculation of 12 revolutions using a time step size equivalent to 10° azimuth steps is sufficient to obtain reasonable accurate results in hover. Next, the tandem rotor operating points investigated experimentally by Stepniewski were simulated using UPM, focusing on the accuracy of the calculated total thrust. The collective pitch angles were set according to the experimental values, while cyclic pitch, flapping and lagging motions were all set to zero. Thus, no trim procedure was needed for these computations. The total static thrust was calculated by averaging the instantaneous thrust values of the last revolution. Figure 4 shows the calculated thrust compared to test data from [6]. For most operating points, the calculated thrust matches the measured data very well. The trends regarding the effect of overlap, collective pitch and rotation velocity on the total static thrust are correctly reproduced. Noticeable deviations are only observed for the points where the rotor operates at the highest tip Mach number. Here, UPM underestimates the rotor thrust. This can probably be attributed to the fact that the calculations were carried out without compressibility correction, although the Mach number effect on the outer sections of the rotor blades is starting to become significant.

Figure 5 shows the calculated wake shapes and the predicted unsteady thrust of the front and rear rotors for -3.65% and 37.5% overlap. It can be seen clearly that the interaction effects increase with a higher overlap, leading to stronger oscillations in the instantaneous thrust of the individual rotors. As expected, the observed oscillation frequency of 3/rev corresponds to the blade passing frequency. The phase shift of 60° and the reversed signal of the front and rear rotor thrust also satisfy the expectations, as the rotors are counter-rotating and intermeshing. The correct prediction of the unsteady behavior of the rotor system can provide valuable information in the predesign stage, as it may lead to vibrations, high control rod loads and high BVI noise levels.

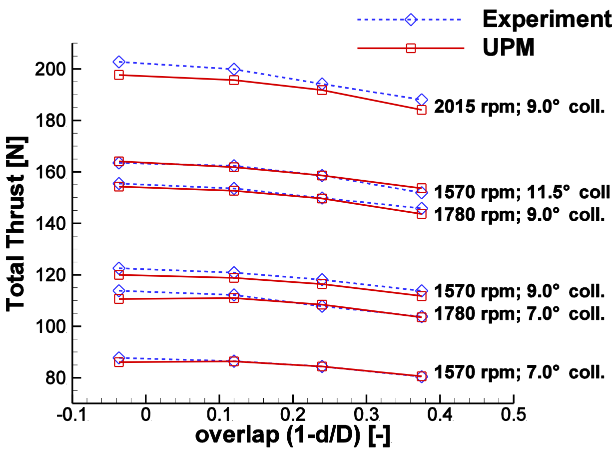

Figure 4: Calculated tandem rotor thrust in hover compared to test data from [6]

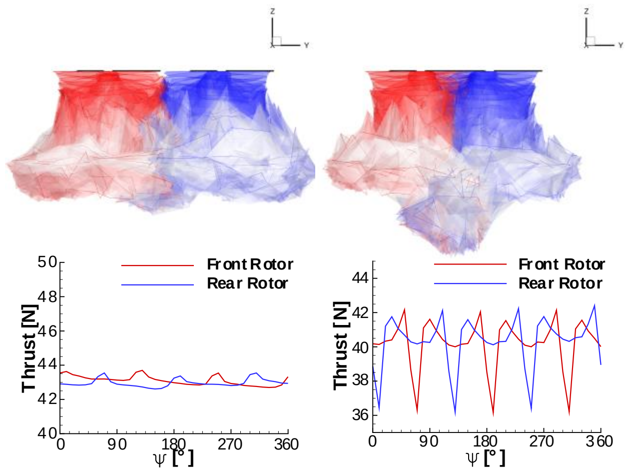

Figure 5: Calculated wake shape and instantaneous rotor thrust for -3.65% and 37.5% overlap at 1570 rpm and 7° collective pitch

4.2. Tandem rotor power in level flight

Next, a test case focusing on the power required by a tandem rotor in level flight, delivering constant thrust at various advance ratios, was selected. Geometry and experimental data from measurements in the Langley full-scale wind tunnel by Dingeldein [7] were used as reference for the validation of this test case. The tandem rotor consists of two coplanar, non-overlapping rotors, each having two rectangular, untwisted blades using NACA0012 airfoils at all sections. Figure 6 and Table 2 show the geometric properties and operating conditions of the rotor in detail.

Table 2: Tandem rotor parameters

Property	Symbol	Value	Unit
rotor distance	d/D	1.03	[-]
vertical separation	$\Delta z/D$	0.0	[%]
number of blades / rotor	N_b	2	[-]
radius	R	2.25	[m]
blade chord length	c	0.19	[m]
taper ratio	λ	1.00	[-]
twist	$\Delta\theta$	0.0	[°]
thrust coefficient	C_T	0.0034	[-]
tip Mach number	M_{tip}	0.44	[-]

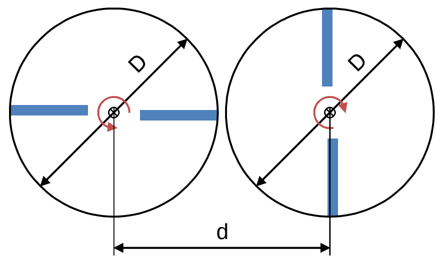

Figure 6: Tandem rotor geometry specifications

Within the UPM simulations, a trimming procedure similar to the method used in the experiment and described in [7] has been implemented. In order to balance the parasite drag of a virtual fuselage with an equivalent flat plate area $f = 0.1858\ \text{m}^2$, the rotor tip path plane is tilted forward. The tip path plane tilt angle α_{TPP} is calculated for each advance ratio μ using the following relation:

$$\alpha_{TPP} = \sin^{-1}\frac{f\mu}{2C_T A} \tag{5}$$

The rotor thrust coefficient C_T and the rotor disk area A are set according to the experiment.

Then, the isolated front rotor is trimmed by adapting its collective and cyclic pitch angles in order to generate 50% of the total tandem rotor target thrust, while not producing any pitching or rolling moments. Finally, the control angles of the front rotor are frozen to these values and the rear rotor is added to the calculation. The rear rotor collective and cyclic pitch angles are then trimmed until the tandem rotor system generates the total target thrust and the rear rotor is free of pitching and rolling moments. The control angles resulting from the UPM calculations using this trim procedure are depicted in Figure 7.

This trimming procedure does not emulate the trimming of a helicopter in free flight, as neither a zero net yawing moment is ensured nor the thrust sharing ratio of the rotors is kept constant (see Figure 8), meaning that the equilibrium about the pitch axis would be established at different longitudinal CoG positions for different advance ratios.

The procedure for the estimation of the profile power described in section 3.2 was used when calculating the total power required. Two profile drag models have been compared: firstly, a constant airfoil drag coefficient $c_d = c_{d0} = 0.01$ was assumed. Secondly, the airfoil drag coefficient was modelled as a function of the local angle of attack, using equation (4). The coefficients were calibrated using Dingeldein's static thrust measurements [7] of the isolated front rotor ($K_0 = 0.0123$, K_1=0.52, α_0=1.68°). The value obtained for K_0 is slightly higher than commonly used experimental profile drag coefficients for the NACA0012 airfoil with standard surface roughness [8], but contains the drag of the rotor hub.

Figure 9 shows the simulation results for the power required by the isolated front rotor, the front and rear rotors in tandem configuration and the total power for the tandem rotor using two different time steps, corresponding to 10° and 5° azimuth. A higher resolution in time improves the simulation results noticeably for high advance ratios, while the results at low advance ratios do not change significantly when using a smaller time step.

The computed power for the front rotor correlates very well with the experimental data, when using the calibrated profile drag model. Only for the data point at the highest advance ratio ($\mu = 0.295$) a noteworthy lower power was measured. Assuming a constant profile drag coefficient $c_d = c_{d0} = 0.01$ leads to an underestimation of the profile power. The power required by the front rotor operated in the tandem configuration differs only marginally from the power required by the isolated front rotor (designated as single rotor in Figure 9). This trend is consistent for the measured and calculated data.

In level forward flight the rear rotor requires considerably more power than the front rotor. This is attributed to the fact that the rotor wake of the front rotor passes partially through or nearby the rear rotor disk, thus inducing significant steady and unsteady downwash velocities in the operating region of the rear rotor. As depicted in Figure 7, the applied trim procedure leads to significantly higher collective pitch angles at the rear rotor, compared to the front rotor, which also explain its increased power consumption. But when compared to the experiment, UPM underestimates the power required by the rear rotor. The reason for this is not clear, as hardly any information is available about the experiment, which would help to further investigate the differences. The static thrust measurements show a substantial increase in profile power of the tandem rotor when compared to the single rotor. This is probably partly responsible for the underestimation of the power required in forward flight. Other possible reasons for the differences could be different trim states, blade loadings and viscous effects, e.g. caused by the rotor hub in the experiment.

Most differences between the measured and calculated total power required by the tandem rotor arise from the underestimation of the rear rotor power. For the hovering tandem rotor, a favorable interference effect was observed in the experiment, resulting in a significantly lower required power, compared to the same rotor operating at low advance ratios. This effect could not be reproduced in the UPM simulation. But other experiments involving hover tests of tandem rotors [9] [10] show an adverse interference effect, as stated by [11]. This indicates, that there might be an error in Dingeldein's data or other effects not considered in the simulations. According to Dingeldein [7], one possible cause is a stronger ground effect of the tandem rotor compared to the single rotor. Furthermore, he states that this favorable interference probably disappears at extremely low forward speeds and is therefore expected not to be of any practical importance.

For the data point with the highest advance ratio the UPM result also deviates from the measured data. A closer look at the experimental data reveals that this difference results from the reduced power required by the front rotor at this advance ratio and is also observed in the isolated rotor test. This may be explained by the onset of compressibility effects on the outer region of the advancing blades not properly captured by UPM.

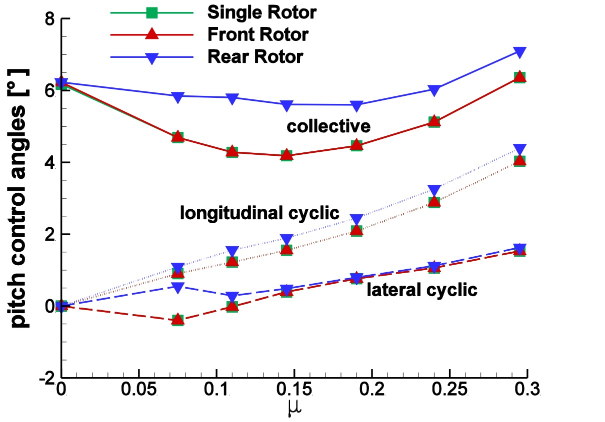

Figure 7: Calculated pitch control angles

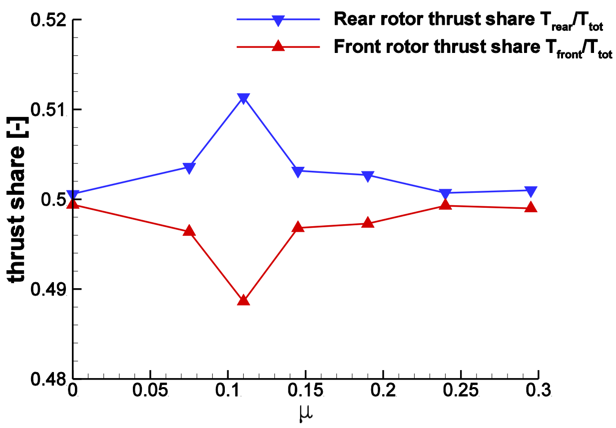

Figure 8: Predicted rotor thrust share

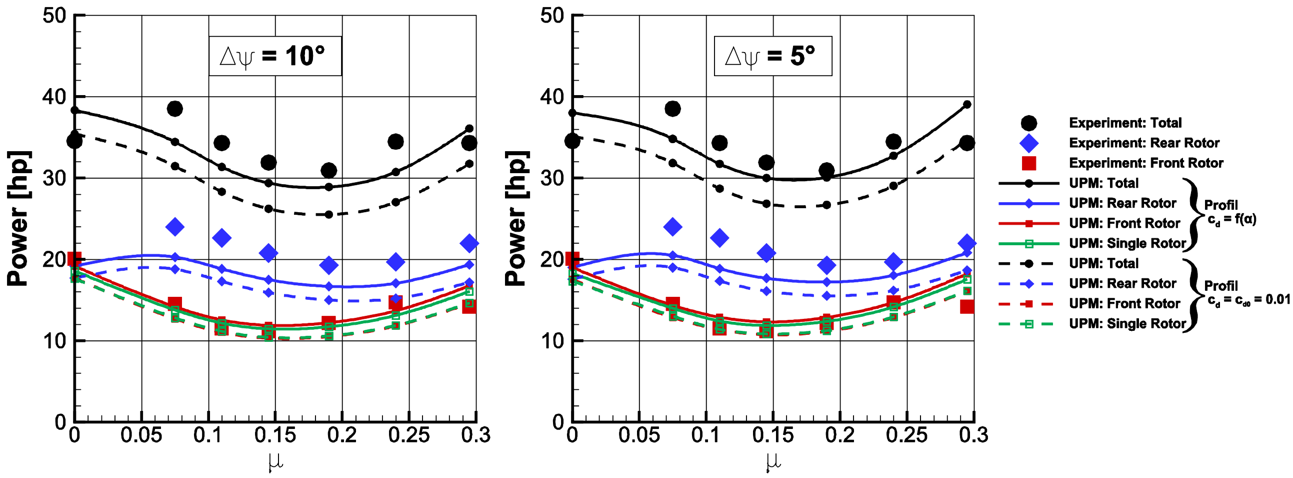

Figure 9: Calculated power required using 10° (l.) and 5° (r.) time steps compared to experiment [7]

Figure 10 shows the wake shapes of the tandem rotor from the UPM simulations for three different points of the calculated power curve.

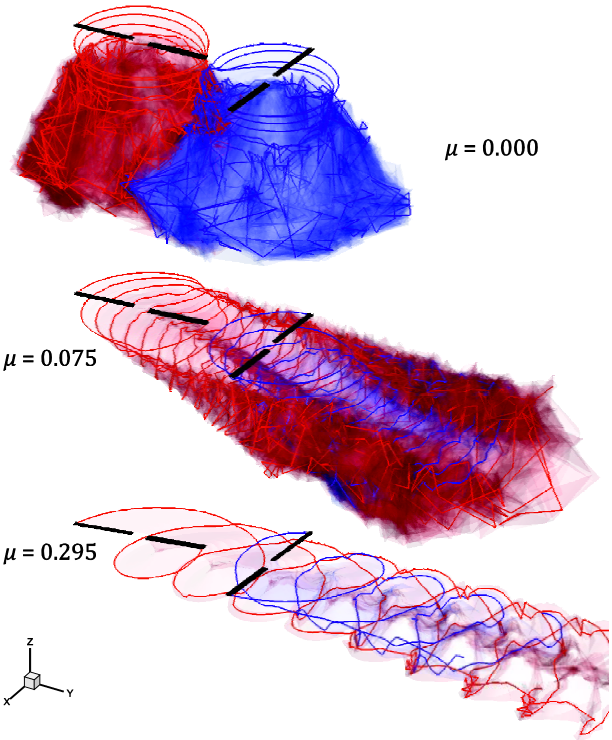

Figure 10: Visualization of the calculated wake of the tandem rotor at three different advance ratios

4.3. Coaxial rotor power in level flight

Besides the tandem rotor, Dingeldein investigated the power required by a coaxial rotor delivering constant thrust in hover and level flight at various advance ratios experimentally [7]. His coaxial rotor tests have also been selected for the validation of UPM. The full-scale coaxial rotor consists of two rotors with 3.75 m radius and a vertical separation of 9.32% of the rotor diameter. The upper and lower rotor each has two tapered blades with a nonlinear thickness distribution plotted in Figure 12. The airfoils used are NACA 4-digit symmetrical airfoils with more than 30% maximum thickness at the root and considerably thinner airfoils at the tip. The rotor geometry, its dimensions and operating conditions are specified in detail in Figure 11 and Table 3.

Table 3: Coaxial rotor parameters

Property	Symbol	Value	Unit
vertical separation	$\Delta z/D$	9.32	[%]
number of blades / rotor	N_b	2	[-]
radius	R	3.75	[m]
blade chord length	$c_{r/R=0.75}$	0.16	[m]
taper ratio	λ	0.33	[-]
twist	$\Delta\theta$	0.0	[°]
thrust coefficient	C_T	0.0048	[-]
tip Mach number	M_{tip}	0.41	[-]

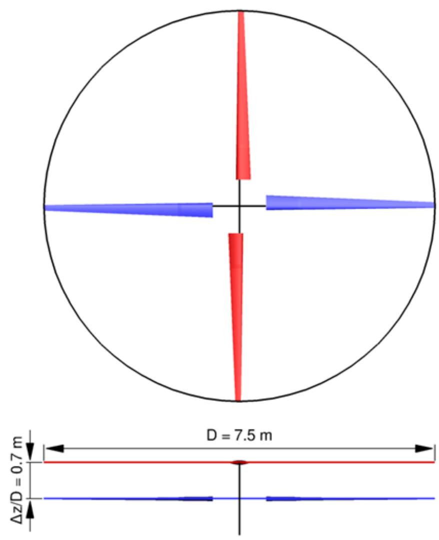

Figure 11: Coaxial rotor geometry specification

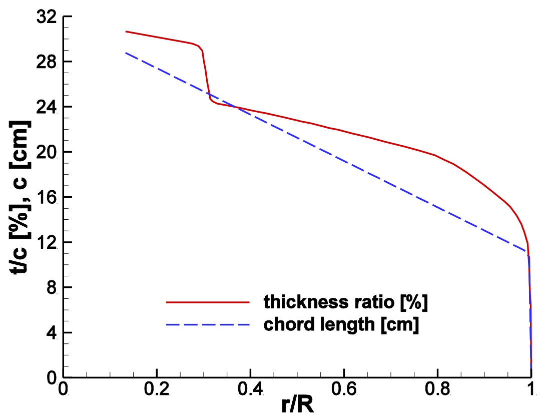

Figure 12: Taper and thickness distributions of the rotor blade used in Harrington's [12] and Dingeldein's [7] coaxial rotor tests

Calculations similar to the previous tandem test case have been carried out, using two different profile drag models (based on equation (2) with $c_{d0} = 0.01$ and equation (4)). The parameters $K_0 = 0.01175$, $K_1 = 0.34$ and $\alpha_0 = 3.47°$ for the profile drag model based on equation (4) were obtained by nonlinear least squares approximation of hover static thrust experimental values for the single rotor from [7]. The static thrust and power results for the single rotor using the second profile drag model are depicted in Figure 13 together with the experimental data. The values of K_0, K_1 and α_0 obtained for the single rotor were also used in the coaxial rotor calculations.

The trimming procedure differed from the tandem rotor case. An equivalent flat plate area $f = 0.9290\ \mathrm{m}^2$ was used to account for fuselage drag and to calculate the tip path plane tilt angle with equation (5). The isolated upper rotor was trimmed to produce half of the total target thrust while not generating any pitching or rolling moments. The collective and cyclic angles were adjusted in order to fulfil the trim conditions. Using the single rotor control angles as initial values, the coaxial rotor was then trimmed with the following trim targets:

- Total target thrust:
  $T_{upper} + T_{lower} = T_{target}$
- Yaw moment equilibrium:
  $M_{z,upper} + M_{z,lower} = 0$
- No pitching or rolling moments on both rotors:
  $M_{x,upper} = M_{y,upper} = M_{x,lower} = M_{y,lower} = 0$

The control angles resulting from the UPM simulations of the isolated upper rotor and the coaxial rotor at different advance ratios are plotted in Figure 14. The collective pitch of the rotors operated in coaxial configuration is notably higher than for the single rotor generating half of the coaxial rotor thrust. This indicates that the rotor efficiency is affected negatively by the interference effects.

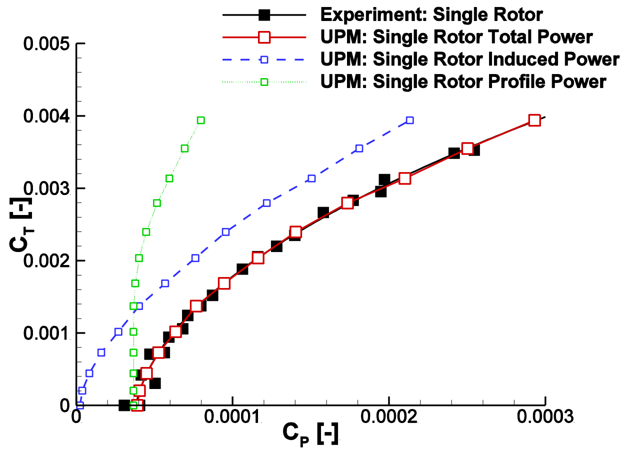

Figure 13: Calibration of the profile drag model using static thrust measurements for the single rotor in hover

The wake shape calculated by UPM is depicted in Figure 15 for three different advance ratios.

Figure 16 shows the UPM results of the total and induced power required for the coaxial and the single rotor at various advance ratios together with the measured total power. The calculated total power for the single rotor using the previously described calibrated profile drag approximation agrees very well with the experimental values, as already seen for the tandem rotor case. The calculated power required by the coaxial rotor is underpredicted by the UPM calculation, but its qualitative dependence from the advance ratio is reproduced very well. A better agreement may be achieved by repeating the profile power approximation using the coaxial rotor experimental static thrust data instead of the results for the single rotor. Using lift curve slope values adapted to the local blade thickness instead of assuming the NACA0012 lift curve slope at all sections might also improve the predicted viscous profile power.

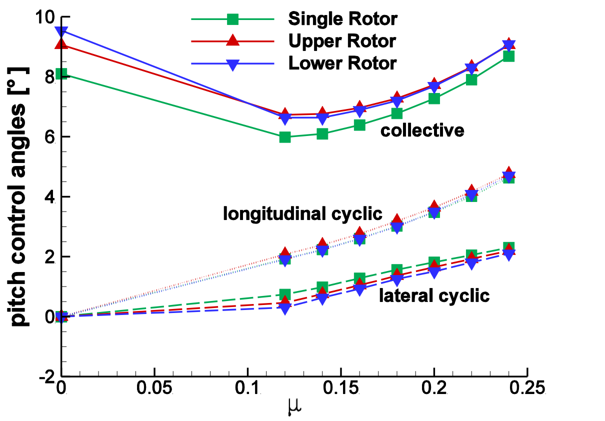

Figure 14: Calculated pitch control angles for the coaxial rotor at various advance ratios

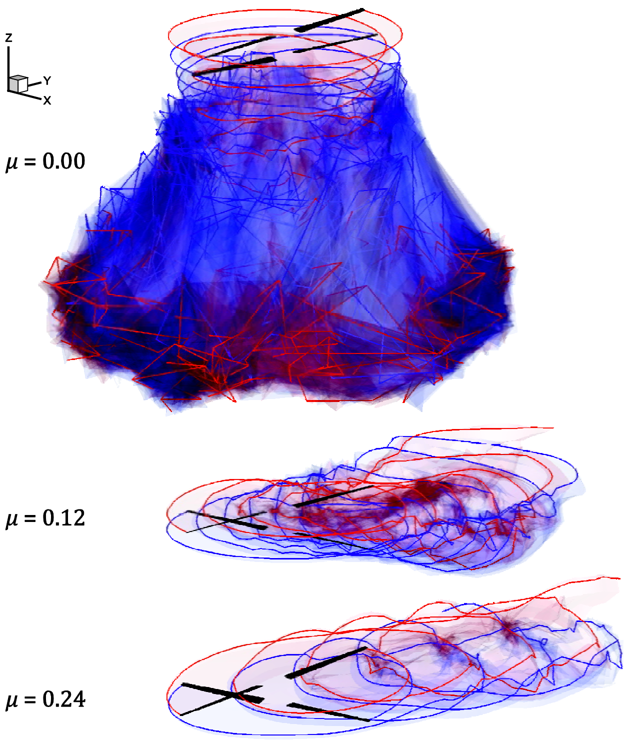

Figure 15: Visualization of the calculated wake of the coaxial rotor at three different advance ratios

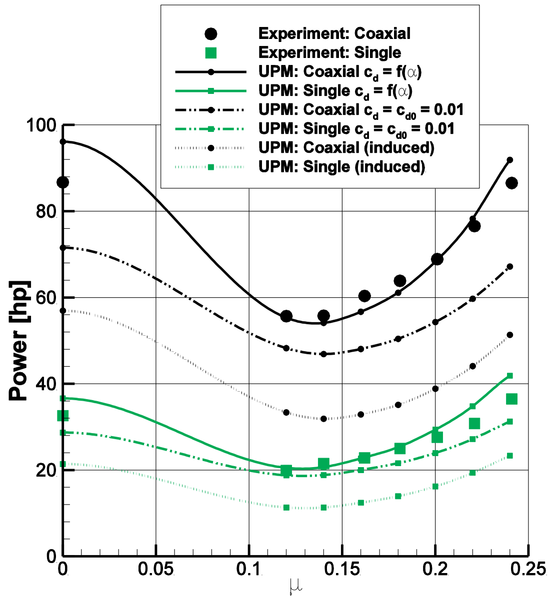

Figure 16: Calculated power required for the coaxial rotor compared to experimental data from [7]

4.4. Rotor-body interaction

Besides rotor-rotor interferences, rotor-body interferences can have a huge impact on loads, flight performance, vibration and noise characteristics of rotorcraft. As the interference effects are greatly influenced by the basic configuration architecture and predesign parameters, they should already be considered in the preliminary design stage. The ability to correctly predict the geometry of rotor wakes in the presence of a fuselage is essential for numerical methods to accurately compute these interference effects and their repercussions, e.g. on rotor inflow and fuselage loads.

The well-known experiments using NASA's ROBIN model fuselage [13] have been selected to assess the UPM code for rotor-body interaction cases. Extensive experimental data are available, including wake geometry [14], inflow velocities above the rotor plane [15] and fuselage surface pressures [13]. Furthermore, there are many publications including numerical results for the ROBIN test cases, thus making them a good base for code comparison and benchmarking. In this paper, the results for the level flight case with an advance ratio $\mu = 0.15$ and a blade loading $C_T/\sigma = 0.064$ are presented.

Table 4: Rotor geometric properties and operating point

Property	Symbol	Value	Unit
number of blades	N_b	4	[-]
radius	R	0.86	[m]
blade chord length	c	0.066	[m]
taper ratio	λ	1.0	[-]
twist	$\Delta\theta$	-8.0	[°]
thrust coefficient	C_T	0.0064	[-]
advance ratio	μ	0.15	[-]
tip Mach number	M_{tip}	0.56	[-]

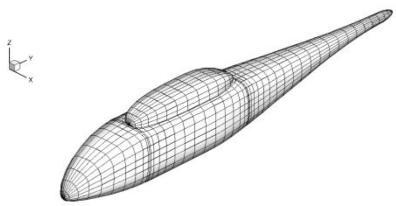

Figure 17: The ROBIN fuselage

Only the main rotor blades and the fuselage were considered in the simulation, additional features like rotor hub, model supports and wind tunnel walls were not modelled. The ROBIN fuselage has a generic, analytically defined shape based on superelliptical sections. It consists of a slender main body and a nacelle mounted in the rotor hub region on top of the main body (Figure 17). A fully articulated rotor with 0.86 m radius was used in the experiments, which were selected for validation. The rotor had four blades with rectangular planform, NACA0012 airfoil section and 0,066 m chord. The blades were twisted linearly by -8°. They were designed to be very stiff, in particular regarding torsion, in order to minimize aerodynamic uncertainties resulting from elastic blade deformation. Thus, the error resulting from the assumption of rigid blades in the simulations should be negligible.

The collective pitch angle for the calculations was determined by UPM's internal trim procedure using the experimentally measured rotor thrust as trim target. The cyclic pitch angles were set according to the experimental values and fixed. Blade flapping was set to zero, as the rotor has been trimmed for no flapping in the experiments.

After the last trim angle adjustment the computation was continued for at least eight rotor revolutions. The calculations were carried out using a time step size corresponding to 5° azimuth and restricting the wake length to eight revolutions.

4.4.1. Wake geometry

Wake geometry measurements were conducted by Ghee using NASA's 2-meter rotor test system (2MRTS) [16] in the Langley 14- by 22-Foot Subsonic Tunnel. The blade tip vortex trajectories were visualized using a laser light sheet combined with injected smoke. The laser sheet was strobed in order to identify instantaneous vortex positions on longitudinal slices cutting vertically through the rotor plane. By varying the phase of the strobe, it was possible to capture the tip vortex locations with the rotor at different azimuth positions.

The method used to extract instantaneous tip vortex positions from the UPM results is very straightforward, as the wake geometry is output by UPM for each time step. The outmost vortex filament

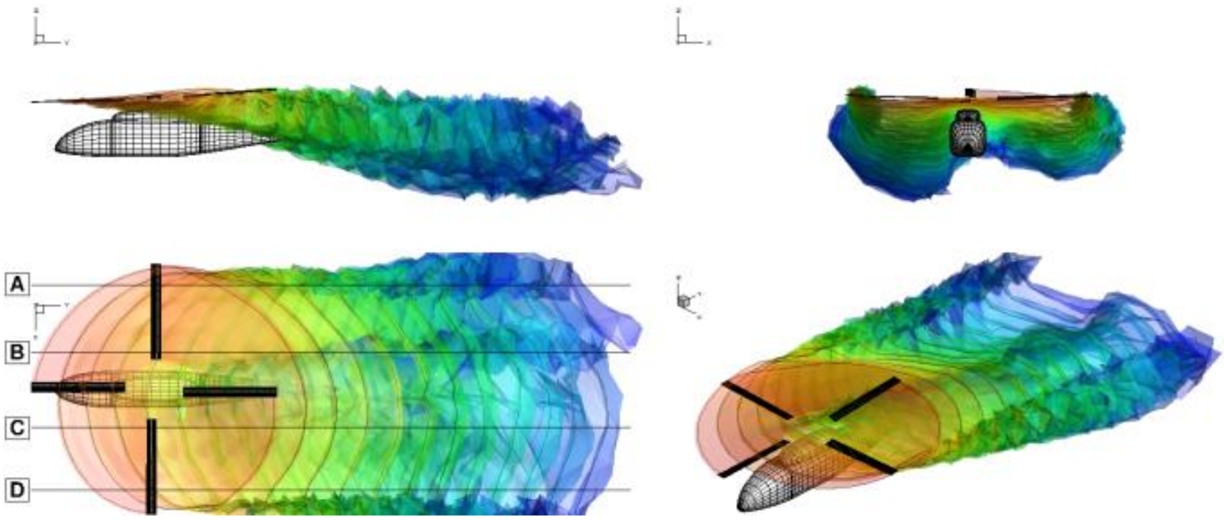

Figure 18: Calculated wake shape for the flight state μ=0.15, C_T/σ=0.064

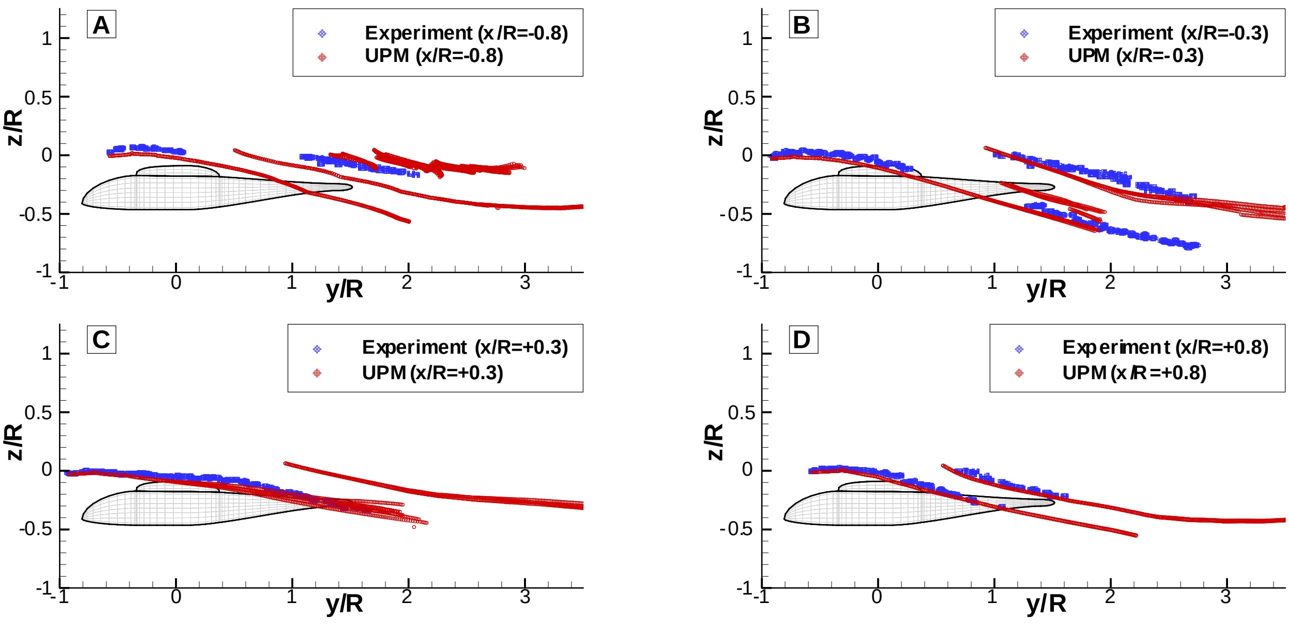

Figure 19: Simulated tip vortex trajectories at four longitudinal slices compared to the locations captured in the experiment

of the wake is regarded as tip vortex trajectory. In order to visualize the vortex paths in longitudinal slices, the intersections of the tip vortex trajectories with the slices are calculated for each time step of the last quarter rotor revolution and merged into one dataset.

Figure 18 depicts the rotor wake calculated using UPM. A strong interaction of rotor and fuselage for this flight state can be observed, as the wake passes in close proximity near the nacelle and wraps around the rear part of the fuselage.

The tip vortex positions extracted from UPM simulation results are displayed in Figure 19 together with measured data. They show a very good accordance, especially for the wake behind the retreating blade side of the rotor. The UPM output includes sampled points for the complete last rotor revolution, thus the wake positions of all four blades were captured. Due to instabilities in the vortex field, the tip vortices of the four blades move on slightly different trajectories. Slice A cuts through the rolled up part of the wake – the comparison with the experimental results suggests that only the upper part of the rolled up vortices was sampled in the experiment.

Other minor differences between the experimental and the simulated results can be seen:

- The upwash at the front part of the rotor is slightly underpredicted by UPM. This behaviour can also be observed in the results of other numerical simulations for this test case, e.g. [17].
- The UPM results show a marginally flatter path of the tip vortex in the region near the rear part of the nacelle (slice C). This might be attributed to the absence of the rotor hub in the simulation or viscous effects in the flow behind the nacelle.

Table 5: Experimental [14] and simulated control angles

Name	Symbol	Exp.	Sim.	Unit
shaft angle	α_s	-3.0	-3.0*	[°]
coning angle	β_0	1.5	1.5*	[°]
collective pitch	θ_0	6.55	6.57	[°]
lateral cyclic pitch	θ_{1s}	-1.39	-1.39*	[°]
long. cyclic pitch	θ_{1c}	1.99	1.99*	[°]

* experimental values [14] used for simulation

The collective pitch angle from the trimmed UPM calculation matches the experimental value almost exactly (see Table 5).

4.4.2. Inflow velocities above rotor plane

Using the ROBIN fuselage with 2MTRS Rotor system, a series of rotor inflow measurements with different rotor blades and advance ratios was conducted by Elliot *et al.* in the NASA Langley 14-by 22-Foot Subsonic Tunnel (e.g. [15]). The instantaneous components of the flow velocity in the longitudinal (freestream) and vertical directions were measured using a dual laser velocimetry (LV) system. Measurements were made at 15 radial and 10 azimuthal locations of a virtual disk parallel to the rotor tip path plane, located 0.75 and 1.15 blade chord lengths above the rotor tip path plane. In this paper, only the results for μ=0.15 at 1.15 blade chord lengths above the rotor tip path plane [15] are shown. The rotor tip path plane was kept constant in the experiment by fixing the rotor shaft angle and trimming the rotor for zero flapping.

Table 6: Experimental [15] and simulated control angles

Name	Symbol	Exp.	Sim.	Unit
shaft angle	α_s	-3.0	-3.0*	[°]
coning angle	β_0	1.5	1.5*	[°]
collective pitch	θ_0	9.37	6.60	[°]
lateral cyclic pitch	θ_{1s}	-1.11	-1.11*	[°]
long. cyclic pitch	θ_{1c}	3.23	3.23*	[°]

* experimental values [15] used for simulation

Although the operating conditions and trim conditions were similar to Ghee's experiment [14] described in the previous section, the collective pitch angle measured by Elliot is considerably higher. There is also a noticeable difference between the longitudinal pitch angles. The reason for this disparity is not clear, as also reported by other authors (e.g. [17]). In contrast, the collective angles calculated by UPM for the two cases are almost identical. The small difference arises from slightly different rotor thrust target values and distinct applied cyclic pitch angles, taken from the experiments.

Nevertheless, a qualitatively excellent agreement between simulation results and experimental data can be seen in the averaged induced velocities normal and tangential to the tip path plane (Figure 20). Considerable quantitative differences can only be observed at 0° azimuth, the region directly downstream of the rotor hub. The experimental values are probably influenced by flow displacement due to the rotor hub and by the rotor hub wake. Both effects were not considered in the UPM simulation. For the averaged tangential flow component the simulation results also agree very well with the measured experimental data. Again, noticeable differences can be observed in the region directly upstream and downstream of the rotor hub. Furthermore, the calculated tangential velocities in the front region of the rotor are slightly higher than the measured averaged induced velocities. The artifacts observed in the experimental results are caused by single very high and probably erroneous values found in the tabulated data [15].

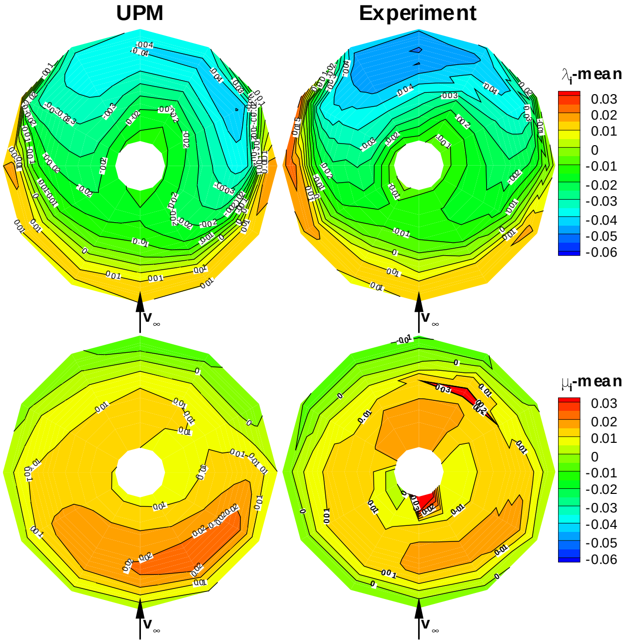

Figure 20: Averaged inflow normal and tangential to the TPP calculated by UPM, 1.15 chord lengths above the rotor disk, compared to measured data from [15]

In Figure 21, the results of the rotor-fuselage calculation are plotted together with the results of an isolated rotor calculation at discrete azimuth positions. The plots clarify the findings observed in the previous figure. The error bars represent the standard deviation of the measured unsteady signal, they do not display the error range of the wind tunnel experiments. Except for 0° azimuth, where the measurement is strongly affected by the rotor hub, almost all calculated average inflow values fit in this range and agree very well with the measured inflow. The influence of the fuselage is minimal for the majority of data points. Only for the line above the fuselage centerline the effect of the fuselage can be seen clearly. Especially the results for the normal component of the induced velocity at $\psi = 0°$ show that the rotor inflow prediction is improved when taking the fuselage into account.

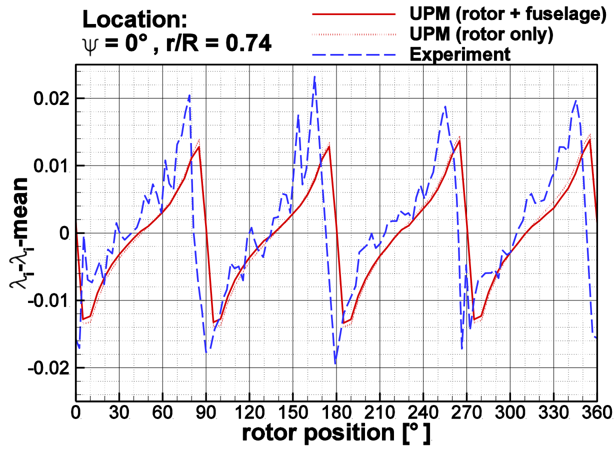

Figure 22: Unsteady induced inflow normal to the TPP at a location 1.15 chord lengths above the rotor disk (ψ=0°, r/R=0.75)

Figure 22 depicts the unsteady induced inflow normal to the TPP at a location in the symmetry plane in the rear of the rotor hub (ψ=0°, r/R=0.74). The amplitude and shape of the calculated signal matches the experiment excellently. It is smoother and contains less variation between the passages of the four blades, when compared to the experimental data. The phase of calculated signal is slightly shifted backwards by a constant offset of about 5°.

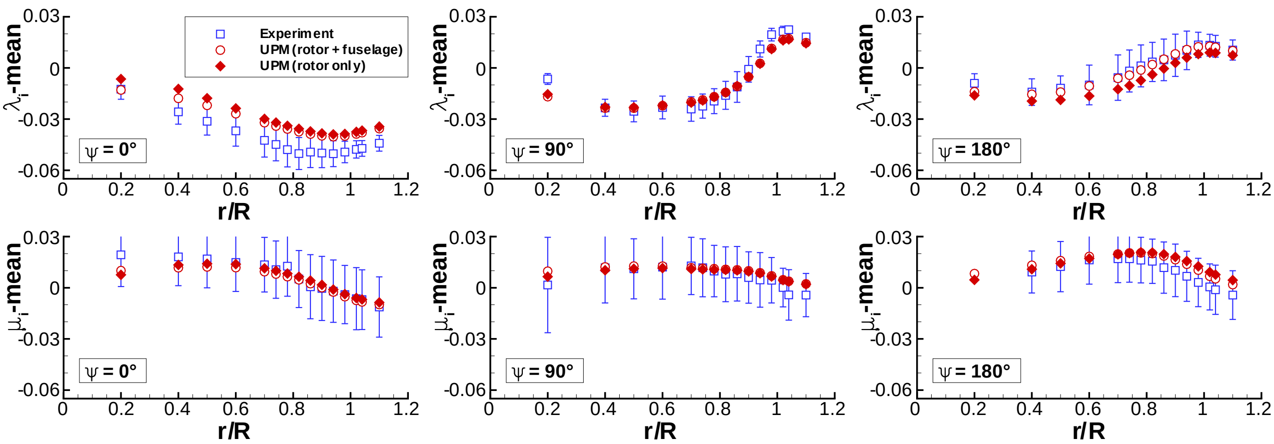

Figure 21: Averaged induced velocities normal and tangential to the tip path plane, 1.15 chord lengths above the rotor TPP, at azimuth 0°, 90°, 180°

5. CONCLUSION AND OUTLOOK

Several test cases were investigated with the aim to evaluate UPM for its suitability to predict interference effects within a preliminary rotorcraft design framework. It became apparent, that an accurate trimming procedure and consideration of the viscous power is essential, when calculating the total power of rotors. The final results correlate very well with the experimental data. In most cases, both steady and unsteady inviscid wake-induced interference effects of rotor-rotor and rotor-fuselage test cases are captured accurately by UPM and the impact of the interference effects on the induced rotor power is qualitatively and quantitatively well predicted. The calculated rotor loads, induced velocities and wake positions also show an excellent agreement with the experiments in most cases.

Overall, these findings encourage the integration and use of UPM in DLR's performance-centric rotorcraft preliminary design environment [18], sketched in Figure 23.

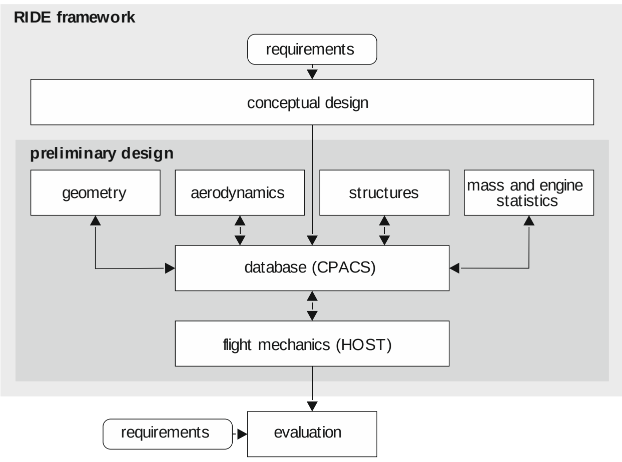

Figure 23: Architecture of the DLR preliminary design framework [18]

The direct integration of UPM as an additional aerodynamics module into the predesign process can be used for the calculation of input parameters for (semi-)empirical interference models built in the flight mechanics code HOST [19] or for the extraction of additional characteristics (e.g. power required, unsteady blade, fuselage, tail or control rod loads, amplitudes and frequencies) from unsteady simulation results, which can be used for the evaluation and comparison of configurations.

Nevertheless, the direct integration method is only viable for the evaluation of individual configurations selected by the user. For the use of UPM within the automatic design and optimization loop, requiring hundreds or thousands of computations in a short time, the computational expense currently seems too high. Therefore, alternative ways of integrating UPM into the preliminary design toolchain are investigated. On the one hand, several options to speed up the UPM calculations without adversely affecting the simulation accuracy are being evaluated. Amongst others, they include parallelization, optimized algorithms (e.g. Fast Multipole Method) and effective trimming procedures. This work will be addressed in a dedicated project in near future. On the other hand, an alternative approach based on the addition of a supplementary surrogate model layer in the design and optimization loop is investigated. It could reduce the total computation time drastically by reducing the number of UPM calculations required in the design and optimization loop and substituting them with the computationally cheap evaluation of the surrogate model whenever possible. Thus, the practical implementation of this approach will be further investigated.

6. REFERENCES

[1] P. F. Sheridan and R. P. Smith, "Interactional aerodynamics - a new challenge to helicopter technology," *Journal of the American Helicopter Society,* vol. 25, no. 1, pp. 3-21, 1980.

[2] J. Yin and S. Ahmed, "Helicopter main-rotor/tail-rotor interaction," *Journal of the American Helicopter Society,* vol. 45, no. 4, pp. 293-302, 1 October 2000.

[3] J. Yin, B. G. van der Wall and G. A. Wilke, "Rotor aerodynamic and noise under influence of elastic blade motion and different fuselage modeling," in *40th European Rotorcraft Forum 2014*, Southampton, UK, 2014.

[4] H. W. Kim and R. E. Brown, "A Rational Approach to Comparing the Performance of Coaxial and Conventional Rotors," *Journal of the American Helicopter Society,* vol. 55, no. 1, p. 12003, 2010.

[5] M. Drela, "XFOIL: An analysis and design system for low Reynolds number airfoils," in *Low Reynolds number aerodynamics*, Springer, 1989, pp. 1-12.

[6] F. D. Harris, "Technical note: Twin rotor hover performance," *Journal of the American Helicopter Society,* vol. 44, no. 1, pp. 34-37, 1999.

[7] R. C. Dingeldein, "Wind-tunnel studies of the performance of multirotor configurations," NACA Technical Note 3236, 1954.

[8] I. H. Abbott and A. E. von Doenhoff, Theory of Wing Sections, New York: Dover Publications, Inc., 1959.

[9] H. H. Heyson, "Preliminary results from flow-field measurements around single and tandem rotors in the Langley full-scale tunnel," National Advisory Comitee for Aeronautics, Washington, 1954.

[10] G. E. Sweet, „Hovering measurements for twin-rotor configurations with and without overlap," NASA, 1960.

[11] M. Ramasamy, "Hover Performance Measurements Toward Understanding Aerodynamic Interference in Coaxial, Tandem, and Tilt Rotors," *Journal of the American Helicopter Society,* vol. 60, no. 3, pp. 1-17, 01 07 2015.

[12] R. D. Harrington, *Full-Scale-Tunnel Investigation of the Static-Thrust Performance of a Coaxial Helicopter Rotor,* 1951.

[13] R. E. Mineck and S. A. Gorton, "Steady and periodic pressure measurements on a generic helicopter fuselage model in the presence of a rotor," NASA/TM-2000-210286. NASA Langley Research Center, Hampton, VA, United States, 2000.

[14] T. A. Ghee, J. D. Berry, L. A. J. Zori and J. W. Elliott, "Wake geometry measurements and analytical calculations on a small-scale rotor model," NASA-TP-3584. NASA Langley Research Center, Hampton, VA, United States, 1996.

[15] J. W. Elliott, S. L. Althoff and R. H. Sailey, "Inflow measurements made with a laser velocimeter on a helicopter model in forward flight. Volume 1: Rectangular planform blades at an advance ratio of 0.15," NASA-TM-100541, 1988.

[16] A. E. I. Phelps and J. D. Berry, "Description of the U.S. Army Small-Scale 2-Meter Rotor Test System," National Aeronautics and Space Administration, Washington, DC, 1987.

[17] A. R. Kenyon and R. E. Brown, "Wake Dynamics and Rotor-Fuselage Aerodynamic Interactions," *Journal of the American Helicopter Society,* vol. 54, no. 1, p. 12003, 2009.

[18] M. Lier, A. Krenik, P. Kunze, D. Kohlgrüber, M. Lützenburger and D. Schwinn, "A Toolbox for Rotorcraft Preliminary Design," in *American Helicopter Society 71st Annual Forum*, Virginia Beach, VA, 2015.

[19] B. Benoit, A.-M. Dequin, K. Kampa, W. von Grünhagen, P.-M. Basset and B. Gimonet, "HOST, a General Helicopter Simulation Tool for Germany and France," in *American Helicopter Society 56th Annual Forum*, Virginia Beach, VA, 2000.

[20] J. Lee, S. Oh, K. Yee and D.-K. Kim, "Numerical Investigation on Overlap Effects of Tandem Rotors in Forward Flight," *International Journal of Aeronautical and Space Sciences,* vol. 10, no. 2, pp. 63-76, 2009.

[21] R. Steijl and G. Barakos, "Sliding mesh algorithm for CFD analysis of helicopter rotor–fuselage aerodynamics," *International Journal for Numerical Methods in Fluids,* vol. 58, no. 5, pp. 527-549, 2008.